HHS Public Access

Author manuscript

Nat Methods. Author manuscript; available in PMC 2024 April 29.

Published in final edited form as:

Nat Methods. 2023 April ; 20(4): 600–609. doi:10.1038/s41592-023-01789-z.

Mesoscale volumetric light field (MesoLF) imaging of neuroactivity across cortical areas at 18 Hz

Tobias Nöbauer[1], **Yuanlong Zhang**[1,2,*], **Hyewon Kim**[1], **Alipasha Vaziri**[1,3,‡]

[1] Laboratory of Neurotechnology and Biophysics, The Rockefeller University, New York, NY, USA

[2] Department of Automation, Tsinghua University, Beijing, China

[3] The Kavli Neural Systems Institute, The Rockefeller University, New York, NY, USA

Abstract

Various implementations of mesoscopes provide optical access for calcium imaging across multi-millimeter fields-of-view (FOV) in the mammalian brain. However, capturing the activity of the neuronal population within such FOVs near-simultaneously and in a volumetric fashion has remained challenging since approaches for imaging scattering brain tissues typically are based on sequential acquisition. Here, we present a modular, mesoscale light field (MesoLF) imaging hardware and software solution that allows recording from thousands of neurons within volumes of ⌀ 4 × 0.2 mm, located at up to 350 μm depth in the mouse cortex, at 18 volumes per second and an effective voxel rate of ~40 Megavoxels per second. Using our optical design and computational approach we show recording of ~10,000 neurons across multiple cortical areas in mice using workstation-grade computing resources.

Information flow across cortical areas is a hallmark of higher-level perception, cognition, and the neuronal network dynamics that underlie complex behaviors. Yet, tracing this information flow in a volumetric fashion across mesoscopic fields-of-view (FOV), at a cellular resolution and at a temporal bandwidth sufficient to capture the dynamics of genetically encoded calcium indicators (GECIs)[1–3], i.e., 10–20 Hz, has remained challenging. While recent advances in two-photon microscopy have enabled a substantial speed-up of the voxel acquisition rate, enabling multi-Hertz cellular resolution volumetric recording of neuroactivity[4], sequential acquisition approaches are intrinsically less scalable to mesoscopic volumes. This is because the volume acquisition rate in serial scanning

‡ Correspondence should be addressed to A.V. (vaziri@rockefeller.edu).

*These authors contributed equally to this work

AUTHOR CONTRIBUTIONS

T.N. designed and implemented the MesoLF optical path under the guidance of A.V., performed experiments, conceptualized, and contributed to implementation of the MesoLF computational pipeline, analyzed data, and wrote the manuscript. Y.Z. contributed to conceptualization and implementation of the MesoLF computational pipeline, performed simulations, analyzed data, and wrote the manuscript. H.K. performed cranial window surgeries and viral injections. A.V. conceived and led the project, conceptualized, and guided the imaging, signal extraction and data analysis approach, designed *in vivo* mouse experiments, and wrote the manuscript.

COMPETING INTERESTS

The authors declare no competing interests.

CODE AVAILABILITY

The custom code that comprises the MesoLF pipeline is available in Supplementary Software 1 under an open source license permitting not-for-profit research use (see file LICENSE.txt) Future updates to the code will be published at http://github.com/vazirilab, together with optical and optomechanical designs and custom C# data acquisition software.

methods scales as the inverse third power of the side length of the imaged volume. In this context, scan-free, parallel volumetric acquisition approaches such as light field microscopy (LFM)[5–12] (and related techniques[13–17]) in which 3D sample locations are mapped onto a 2D sensor offer more favorable scalability to mesoscopic volumes while achieving neuron-level discrimination.

In LFM, encoding of the 3D sample voxels onto the 2D camera sensor is achieved by a microlens array placed in the image plane of a microscope. These sensor images are subsequently computationally reconstructed using the system's point-spread-function (PSF) to obtain 3D sample information. Thus, LFM offers the capability to scale up the acquisition volume both laterally and axially without sacrificing frame rate and thus, in principle, can enable fast mesoscopic volumetric imaging. However, due to the limitations imposed by scattering tissues and the computational cost of large-scale deconvolutions, the use of LFM has remained restricted to only sub-millimeter FOVs and weakly scattering specimen.

We previously extended LFM into the scattering mammalian brain[18,19] by exploiting the strongly forward-directed nature of light scattering in brain tissue and the capability of LFM to capture both angular and lateral position information contained in the incoming light field. Our Seeded Iterative Demixing (SID) approach[18,19] can capture the remaining directional information present in the scattered light-field and, together with the spatiotemporal sparsity of neuronal activity, exploit this information to seed a machine learning algorithm that provides an initial estimate of the locations of the active neurons. SID then iteratively refines both the position estimates and the neuronal activity time series, thereby allowing for neuron localization and extraction of activity signals from depths up to ~400 μm in the mouse brain. LFM's simplicity and scalability combined with SID's potential to extend this approach into scattering brain tissues makes LFM attractive for mesoscale volumetric recording of neuroactivity.

However, practical experimental realizations of mesoscopic LFM imaging in the mammalian cortex have thus far been hampered by a lack of solutions for capturing mesoscopic, multi-millimeter FOVs at high optical resolution, and of computational tools that are suitable for mesoscopic FOVs. In addition to SID's capability to extract signals in the presence of scattering, such computational tools must be able to address the unique challenges associated with faithful localization and extraction of neuronal signals at such scale, such as varying tissue morphology and non-rigid tissue deformation, while keeping computational cost at bay despite terabyte-scale raw data sizes.

RESULTS

Mesoscale high-speed volumetric functional imaging in mouse

Here we demonstrate a modular Mesoscale Light Field (MesoLF) imaging hardware and software solution that combines mesoscale optical design and aberration correction with a scalable computational pipeline for neuronal localization and signal extraction. We demonstrate volumetric recording from more than 10,500 active neurons across different regions of the mouse cortex within different volumes of ⌀ 4 × 0.2 mm positioned at depths up to ~400 μm at 18 volumes per second, over timespans of up to half an hour per

recording (Supplementary Fig. 1) and exceeding one hour when recording from a series of depths subsequently at the same lateral location. In contrast to imaging methods that rely on scanning, all voxels within each volumetric frame are acquired simultaneously. A single mid-range workstation was sufficient to perform signal extraction, localization and demixing from a 7-minute recording (~700 GB raw data size) in 24 hours. In contrast to other computational pipelines for spatiotemporal signal extraction which rely on large-scale matrix factorizations, the runtime of our pipeline scales approximately linearly with recording duration and can be parallelized efficiently across multiple cores and nodes in a cloud computing environment or an on-premises cluster. It thereby scales to large FOV sizes and recording durations.

We have designed the MesoLF optical system to be compatible with a widely used commercial mesoscopy platform[20] which was originally conceived for multiphoton scanning microscopy but lacks well-corrected wide-field imaging capabilities. To implement MesoLF we designed and incorporated a custom tube lens in the optical detection path (Supplementary Note 1, Supplementary Fig. 2). Our custom tube lens consists of three doublet elements in a configuration akin to the Petzval objective design form[21]. The elements were numerically optimized to correct the output of the mesoscope objective to achieve diffraction-limited imaging of a ⌀4-mm-FOV at NA 0.4 and 10× magnification in the 515–535 nm emission range of GCaMP calcium indicators. Thereby we achieved a widefield (pre-LFM) optical resolution of ~600 line-pairs per millimeter across the entire FOV, thus enabling a wide range of high-resolution mesoscopy applications other than LFM, which are often limited by insufficient resolution in large-FOV optics.

To facilitate LFM recording, we placed a microlens array into the image plane of our custom-designed tube lens. An 80-Megapixel CMOS camera captures the resulting raw LFM images at 18 Hz. All optical components of the MesoLF system, including the 470 nm LED illumination arm, form a module that was integrated into the optical path of our mesoscope via a motorized fold mirror.

The MesoLF computational pipeline (Fig. 1, Extended Data Fig. 1–6, Supplementary Notes 2–10, Supplementary Fig. 3–6, Supplementary Video 1, Supplementary Software 1, additional online data[22]) is engineered from the ground up to maximize localization accuracy and signal extraction performance at depth in scattering tissue and addresses challenges associated with scaling the current LFM reconstruction approaches[6,7] to mesoscopic volumetric FOVs. Briefly, after tiling the FOV into 6 × 6 patches, correcting for sample motion, subtracting the global dynamic fluorescence background, and masking vasculature, the MesoLF pipeline generates a temporally filtered activity summary image in which the weakly scattered LFM footprints of active neurons are emphasized relative to the strongly scattered background. A background-rejecting phase-space-based LFM deconvolution approach generates a volumetric estimate of the locations of the active neurons while rejecting fluorescence background from above and below the imaged volume. Subsequent morphological segmentation allows shape-based identification of neuron candidates and their surrounding volumetric neighborhoods (“shells”) to be used for neuropil subtraction, and the expected footprints of these neuron and shell candidates in the LFM raw data are computed. At the core of the pipeline lies an iterative demixing

step in which the spatial and temporal components are alternatingly updated while keeping the respective other fixed. Signals from core and shell components are demixed and subtracted, and finally, the resulting traces are classified based on their temporal shape using a convolutional neuronal network to reliably identify traces compatible with GCaMP transient characteristics with high signal-to-noise ratio (SNR).

We verified the *in vivo* performance of our high-resolution MesoLF optical module and signal extraction pipeline by performing up to hour-long calcium imaging in the cortex of head-restrained mice exposed to whisker stimulation. Using mice expressing a modified version of the SomaGCaMP7f[23] calcium indicator, we detected ~10,582 active neurons in the depth range of 0–200 μm, 8,076 active neurons in the depth range of 100–300 μm, and 4,746 active neurons in the range of 200–400 μm during ~7-minute recordings of a volumetric FOV of ⌀ 4 × 0.2 mm^3 imaged at 18 Hz (Fig. 2, Supplementary Video 2). The imaged volume contained all or the majority of the posterior parietal, primary somatosensory, primary visual, anteromedial visual, and retrosplenial cortical area. In the extracted temporal signals, clear correlation between bursts of activity and whisker stimulation onsets are observable (Fig. 2b, c).

In 31 recordings from 6 mice, MesoLF detected 5241 ± 3887, 5000 ± 3028, 2387 ± 1744 (mean ± SD) active neurons in the depth ranges 0–200, 100–300 and 200–400 μm, respectively (Supplementary Table 1). The maximal neuron numbers as well as variability across animals are determined primarily by the expression uniformity and coverage across the MesoLF FOV that was achievable by our multi-site viral injection approach as well as the natural variability of blood vasculature. We anticipate that using transgenic lines should markedly improve uniformity of expression.

Pipeline modules for high-quality neuronal signal extraction

The neuron detection sensitivity, signal extraction quality, and neuron localization accuracy at depth in LFM is ultimately limited by reconstruction artifacts due to scatter-induced aberrations and by crosstalk between neurons, neuropil, and out-of-volume fluorescence. In MesoLF, we have addressed these limitations through the following four key conceptual advances (Fig. 1):

First, to reduce reconstruction artifacts that are typical of conventional LFM reconstructions[6,7] – in particular those affected by light scattering – without resorting to computationally costly regularization constraints, the input data is transformed into a phase-space representation. In this representation, the different angular views of the source volume encoded in an LFM raw image are treated separately and thus can be filtered, weighed, and updated in an optimized sequence[11] (Fig. 3a). In addition, we introduce a “background peeling” algorithm in which fluorescent contributions from above and below the target volume are estimated and subtracted. Such out-of-volume background fluorescence is a limiting factor of the performance of reconstruction algorithms. Phase-space reconstruction together with background peeling visibly reduces artifacts compared to conventional LFM reconstruction[6,7] as well as to a previously published phase-space reconstruction approach[11] (Fig. 3b). Quantitatively, the structure similarity index measure (SSIM) (Supplementary Note 5) between reconstruction and simulated ground truth for a depth range of 300–400

μm is reduced by 88% and the neuron localization error by 64% (Fig. 3c–e). The neuron identification precision is improved by 42% and sensitivity by 144% (Extended Data Fig. 3, Supplementary Notes 4–5, Supplementary Fig. 4–5).

Second, the implementation of our morphology-based segmentation (Fig. 3f–h, Extended Data Fig. 4, Supplementary Note 6) allows for applying priors on neuron shape, enabling robust processing of volumes with dense neuron content (Fig. 3f). Compared to the spatiotemporal matrix factorization approaches that have previously been used[24,8], our purely shape-based segmentation approach is not prone to artifacts from segments containing multiple neurons with highly correlated temporal activity as it does not rely on temporal independence (Fig. 3g). Overall, it achieves superior neuron segmentation performance relative to the spatial segmentation solution contained in a comparable one-photon signal extraction algorithm[25] (Fig. 3h). Since segmentation is performed on the reconstruction of the filtered temporal activity summary image, the blurring effects induced by scattering are strongly suppressed. We have optimized these reconstruction and segmentation steps using simulations of a realistic optical tissue model[26] (Extended Data Fig. 3–4, Supplementary Notes 3–6, Supplementary Fig. 3–4).

Third, we devised a local demixing approach to suppress crosstalk from neighboring neurons and eliminate neuropil contamination. While soma-localized GCaMP confines expression to the cell body, residual expression in neurites is still possible. To mitigate such residual neuropil signal, for each detected neuron candidate, a spherical shell surrounding the neuron is generated, and both the neuron and shell are convolved with the ballistic LFM PSF to generate a library of initial LFM footprints (Fig. 3i). The spatial and associated temporal components are then alternatingly refined in a LASSO-constrained optimization[27] (Supplementary Note 8). The spherical shells are included in the demixing so that they can accommodate the local background that arises from crosstalk from neighboring neurons and neuropil. After the main demixing stage, these local background contributions are demixed from the temporal components through a greedy search approach (Supplementary Note 8, Extended Data Fig. 6). Thereby we reduced the average absolute correlation between signal pairs by 37% and effectively reject unphysiological correlations in the extracted signals (Fig. 3j–k).

Finally, to further reject signals arising from non-neuronal sources, such as blood vessel pulsation and residual motion, we classified the candidate traces based on whether their temporal activity patterns are compatible with the known response characteristics of GECIs. We designed and trained a convolutional neuronal network (CNN) on a hand-curated dataset in two different modes, one that emphasizes high sensitivity and one that prioritizes precision, both while maintaining overall high F-score (Fig. 3l–m, Supplementary Note 10, Supplementary Fig. 6). Our CNN achieves a classification performance (F-score) of 93% (Fig. 3n, sensitive mode).

Mitigating mesoscale contaminants in mammalian brain

Scaling computational functional imaging at neuronal resolution from sub-millimeter to mesoscopic FOVs in the mammalian brain poses challenges related to both the intrinsic properties of brain tissue at multi-millimeter scale and the computational scale of the

task. Relative displacements due to non-rigid deformation of the brain that arise from animal motion can be as high as ~10 μm when imaging the brain over multi-millimeter distances. Furthermore, while large blood vessels can usually be avoided in methods covering smaller FOVs, mesoscopic FOVs will always contain several large vessels, which cause, if unmitigated, non-rigid deformation and pulsating shadowing effects that will result in false neuronal signals.

In our MesoLF pipeline, we have addressed these challenges as follows (Fig. 1): Performing non-rigid motion correction in LFM has previously been hampered by the computational cost of frame-by-frame reconstruction as would be required to make LFM data compatible with established motion correction algorithms. We overcame this limitation by performing non-rigid motion correction on raw LFM data and by transforming them into a phase-space representation. We then corrected for motion and deformations of the phase space slice corresponding to the oblique perspective and applied the same correction to each of the other phase space slices (Fig. 4a–c, Extended Data Fig. 1, Supplementary Note 2).

To avoid artifacts generated by the periodic pulsation of the vasculature, we implement a four-pronged approach (Supplementary Note 9): First, blood vessels are detected and masked based on their tubular shape[28] (Fig. 4d). Second, all single-pixel time series are filtered to remove low-frequency oscillations originating from pulsation. Third, remaining spatial features that originate from blood vessel motion are rejected during morphological segmentation based on their shapes. Finally, the aforementioned CNN-based time series classifier serves to further reject blood vessel artifacts.

In MesoLF, the FOV area and hence raw dataset sizes are up to ~64× larger than in our previous LFM-SID systems[18,19] when imaging at the same frame rate. Thus, to enable practical applications of our method, we strongly optimized the computational efficiency of our MesoLF pipeline. To this end, we devised an accelerated and parallelized scheme that employs a custom GPU-based implementation of the most performance-critical function, a special convolution-like operation required for propagating a light field from the sample to the LFM camera and vice versa (Eq. 9 in Supplementary Note 4, Supplementary Software 1; used between step (viii) and (ix) in Fig. 1 to generate the initial set of soma and neuropil spatial footprints). MesoLF thus alleviates this bottleneck, enables scaling to larger and longer recordings with limited GPU resources. In addition, the full FOV is sub-divided into 6 × 6 overlapping tiles that can be processed in parallel on multiple GPUs and subsequently merged to avoid duplicate neurons. When compared to the current release of our SID algorithm[18] (which already requires three orders of magnitude less computation time than conventional frame-by-frame reconstruction of LFM recordings[7,18]), MesoLF can be efficiently parallelized to many CPUs and nodes in a cloud computing environment and achieves a 2.7-fold speed-up in CPU core-hours and a 20-fold speedup in GPU runtime at the same computational resources, while performing a range of qualitatively new functionalities and achieving a quantitatively better performance. MesoLF thus elevates neuron-resolved, fast computational imaging capacity to the mesoscopic scale.

Simultaneously acquired functional ground truth validations

To perform a direct and quantitative validation of performance and accuracy of the MesoLF pipeline in terms of neuron detection performance, neuron localization error and fidelity of extracted neuronal signals we pursued two complementary ground truth validation strategies: First, we temporally interleaved MesoLF detection under volumetric one-photon illumination with planar 2pM imaging. In this “temporally interleaved” verification approach (Fig. 5), the 2pM ground truth data is acquired only in a single plane within the full MesoLF volume. Fast alternation between one- and two-photon excitation every 7 ms allowed us to acquire 2pM and MesoLF signal near-simultaneously on the time scale of calcium indicator dynamics. The key advantage of this approach lies in the use of one-photon volumetric excitation, so that the experimental MesoLF data directly contains the same out-of-volume fluorescence as is present in standard MesoLF acquisitions. However, this method remains fundamentally limited to ground truth verification in a single plane within the full MesoLF volume.

In a second, complementary ground truth verification approach, we computationally combined series of eight planar, simultaneously acquired 2pM–MesoLF functional recordings each to form a total of five volumetric 2pM–MesoLF functional datasets covering the entire depth range of our method (Supplementary Fig. 8, Supplementary Notes 11–12).

In both verification strategies, we established the corresponding ground truth data by automated signal extraction from the 2pM data using the well-established CaImAn signal extraction package[29], followed by manual annotation.

We further corroborated both ground-truth verification results by performance quantifications of both, the full MesoLF pipeline (Supplementary Fig. 10–11) and its individual modules (Fig. 3–4, Extended Data Fig. 2–6, Supplementary Fig. 3–6) on realistic simulated data informed by cortical morphology and physiology (Supplementary Note 5, Supplementary Fig. 3), by statistically comparing MesoLF recordings with subsequent 2pM recordings (Supplementary Fig. 7), and by verifying the presence of visual orientation tuning (Supplementary Fig. 12).

Comparing the “temporally interleaved” ground truth dataset to the output of our MesoLF pipeline applied to the simultaneously acquired volumetric LFM data (Fig. 5a–b), we found that the performance scores sensitivity (true positive rate), precision (positive predictive value) and F-score (harmonic mean of sensitivity and precision) for neuron detection reach values of 0.74 ± 0.12, 0.75 ± 0.12, 0.74 ± 0.11 (mean ± std. dev.), respectively, across the examined depth range (50–400 μm) (Fig. 5b), comparable to the performance achieved by other widely used signal extraction algorithms such as Suite2p[30] and CaImAn[29], applied to planar 2pM data (cf. Ref. [31] for a performance comparison). The F-score consistently exceeds 0.7 up to depths of 350 μm, which we regard as a practical depth limit of the method under the examined conditions. Examination of example neurons and their time series for the two modalities at different depths were consistent with this result (Fig. 5a). The MesoLF pipeline also offers an optional enhanced segmentation algorithm that boosts the sensitivity for detecting the least active neurons, and the separability of neurons that overlap strongly

in space, at the expense of additional computational cost (Supplementary Note 7, Extended Data Fig. 5).

The mean neuron localization error (Fig. 5c) across all depths is 3.8 ± 2.8 μm laterally (mean ± SD), indicating good neuron localization performance on the scale of the typical neuron size.

We investigated the temporal matching of the extracted neuronal traces against our volumetric 2pM functional ground truth and found a temporal correlation between MesoLF and ground truth traces of 0.71 ± 0.26 (median ± SD, n = 353) across all depths (Fig. 5d).

To identify and quantify any artifacts introduced by imperfect demixing of neuronal signals and suppression of background as a function of spatial separation of neurons, we compared the pairwise correlations between pairs of neurons found in ground truth (i.e., physiological correlations) as a function of their lateral distances to the pairwise correlations of the corresponding pairs found in MesoLF-extracted activity traces (Fig. 5e–f). We found no substantial difference between the correlations in the MesoLF-extracted traces and the ground truth trace pairs, regardless of pair distance (Fig. 5e).

To investigate the depth dependence of these pairwise correlations, we computed the excess correlation, defined as the difference in pairwise correlation between ground truth neuron pairs and the corresponding MesoLF neuron pairs (Fig. 5f). At all depths, the modulus of the median and the standard deviation of the excess correlation values were below 0.06 and 0.18, respectively indicating robust demixing and discrimination of neuronal signals.

We also examined MesoLF's performance in extraction of individual calcium transients as a function of depth compared to simultaneously acquired planar 2pM ground truth data in the "temporally interleaved" verification modality based on manual identification of transients by human experts in both modalities. We found values for precision, sensitivity, and F-score of 0.82 ± 0.17, 0.87 ± 0.16, 0.83 ± 0.14 (mean ± SD), respectively, across our depth range (50–400 μm) (Fig. 5g, Supplementary Fig. 9), demonstrating good transient extraction performance at all depths.

The analysis of the "volumetric" ground truth verification dataset yielded comparable performance statistics (Supplementary Note 12, Supplementary Fig. 8) to the "temporally interleaved" modality (Fig. 5) and allowed us to evaluate the axial neuron localization error (Supplementary Fig. 8d), for which we found a mean value of 8.0 ± 4.8 μm (mean ± SD), indicating very good neuron localization performance.

DISCUSSION

MesoLF accomplishes mesoscopic high-speed functional imaging of up to 10,500 neurons within volumes of ⌀ 4 × 0.2 mm located at up to ~400 μm depth at 18 volumes per second in the mouse cortex. This is made possible by realizing the potential for scalability inherent to LFM through a custom optical design, in combination with a set of algorithmic innovations that scale the computational pipeline's capacity and capabilities accordingly.

Through its combination of FOV size and scalability of acquisition speed, MesoLF-based technology is positioned to reach the higher temporal bandwidth (>500 Hz) offered by genetically encoded voltage indicators[32,33], across large volumes in scattering tissue. The achievable frame rate in MesoLF is limited by the number of photons that can be detected per frame while keeping the excitation power and resulting bleaching rate sufficiently low. MesoLF performance will therefore benefit from cameras with improved quantum efficiency, reduced read noise, and faster readout speeds. Here we have shown the performance of MesoLF using GCaMP at up to ~400 μm depth in the scattering mouse brain, limited by loss of directional information of the scattered photons. The obtainable depths can thus be expected to be further increased in the future by using more efficient and red-shifted indicators.

While several aspects of the MesoLF pipeline are specifically designed to tackle issues arising from large-FOV imaging, the general performance improvements afforded by our implementation will also benefit smaller-scale LFMs, such as our head-mounted MiniLFM device[19]. The MesoLF optical and optomechanical design will be available under an open-source license and the custom tube lens will be commercially obtainable, thus lowering the entrance barrier to performing long-duration and high-throughput recording of volumetric calcium activity at mesoscopic FOVs.

METHODS

Experimental model and subject details

All animal procedures met the National Institutes of Health Guide for Care and Use of Laboratory Animals and were approved by the Institutional Animal Care and Use Committee (IACUC) at The Rockefeller University, New York (protocol number 15848H).

Mice were obtained from The Jackson Laboratory (C57BL/6J) and typically group-housed in standard cages with a maximum of 5 mice per cage. Cages were housed in an environment with a 12/12 h reverse dark/light cycle, and ambient temperature of 72 °F and an ambient humidity of ~30%. Mice were provided food and water *ab libitum.*

Virus injection and cranial window surgery

Mice were anesthetized with isoflurane (1–1.5% maintenance at a flow rate of 0.7–0.9 l/min, RWD Life Science anesthesia machine) and placed in a stereotaxic frame (Kopf Instruments). Dexamethasone (0.4 mg/ml) was administered subcutaneously to manage brain swelling. A ~1 cm incision was made over the midline of the scalp and the underlying periosteum was cleared from the skull. The scalp was sterilized, then removed after administration of local anesthetic bupivacaine (0.125 mg/ml), and the underlying connective tissue was cleared from the skull. A custom-made stainless-steel head bar was fixed behind the occipital bone with cyanoacrylate glue (Loctite) and covered with black dental cement (Ortho-Jet, Lang Dental). Circular craniotomies (5 mm diameter) were performed over the desired imaging site.

A glass pipette was first back-filled with mineral oil and then front-filled with a genetically expressed calcium indicator adeno-associated virus (AAV9-syn-jGCaMP7s-WPRE; cocktail

of AAV9-TRE3–2xsomaGCaMP7f & AAV1-Thy1-tTA; AAV1-hSyn1-GCaMP6f). The pipette was then slowly lowered to each injection site and virus was injected (100–125 nl per site, at 10–25 nl/min; titer 2×10^{12}–2.6×10^{13} vgs/ml) into the brain parenchyma at 200 μm depth (single injection; up to 5 × 5 grid of injections centered at PPC: −2.5 mm AP, 1.8 mm ML, 0.2 mm DV or 0.4 mm DV). During multiple injections, the exposed brain was soaked under cold sterile saline.

After virus injection, a circular 5-mm glass coverslip (#1 thickness, Warner Instruments) was lowered into the craniotomy site and sealed in place with tissue adhesive (Vetbond). The exposed skull surrounding the cranial window was covered with a layer of cyanoacrylate glue and then dental cement.

Post-operative care consisted of 3 days of subcutaneous delivery of meloxicam (0.125 mg/kg), antibiotic-containing feed (LabDiet #58T7), and meloxicam-containing (0.125 mg/tablet) food supplements (Bio-Serv #MD275-M). After surgery, animals were returned to their home cages and were given at least one week for recovery and viral gene expression before being subjected to imaging experiments. Mice with damaged dura or unclear windows were euthanized and were not used for imaging experiments. Supplementary Table 1 lists animals, preparation and imaging parameters used in this study.

In vivo Ca^{2+} imaging with MesoLF optical system

For MesoLF imaging, animals were head-fixed on a home-built treadmill underneath the HHMI Janelia/Thorlabs 2p-RAM mesoscope objective. The headbar clamp pair was mounted on a two-axis goniometer stage for precision tip/tilt adjustment. Using this goniometer and the 2p-RAM motorized gantry axes (x, y, z, tilt), the cranial window was adjusted to be orthogonal to the optical axis of the 2p-RAM objective. This was achieved using a home-built alignment tool that can be placed into the objective mount and provides a laser reflex from a reference glass plate that is used as the target for aligning the laser reflex from the cranial window.

The MesoLF optical system used for Ca^{2+} imaging is described in detail in Supplementary Note 1 and Supplementary Fig. 2. Briefly, for MesoLF imaging, a motorized fold mirror was moved into the 2p-RAM emission arm to direct fluorescence towards our custom-built MesoLF path and also reflect incoming one-photon excitation light from the MesoLF path towards the 2p-RAM objective.

The MesoLF excitation path consists of a mounted blue LED (Thorlabs M470L3, 470 nm center wavelength, 650 mW), adjustable asphere collimator (Thorlabs SM2F32-A), an iris aperture for adjusting illumination NA, excitation filter (Chroma ET470/40x, ⌀ 2”), engineered diffuser for creating a flat-top intensity profile (RPC Photonics EDC-10–15027-A 2S, 2” square), relay lens (Edmund 45–418, f=300, ⌀ 3”) and three fold mirrors. This arrangement provides telecentric, homogeneous illumination in the focal plane in the sample. Illumination power was ~15 mW post-objective, which corresponds to ~1.2 mW/mm^2, a value comparable to our previous LFM imaging methods and typical wide-field imaging protocols.

The MesoLF emission path consists of an emission filter (Semrock Brightline FF01–525/39, ⌀ 2”), microlens array (RPC Photonics MLA-S100-f12, square grid, pitch 100 μm, f = 1.2 mm, F-number 12.5, diced to 42 × 42 mm) and camera (Teledyne DALSA Falcon 4-CLHS 86M, 86 Megapixels, 6 μm pixel pitch, 12 bit, global shutter, 16 fps full frame rate). The excitation and emission paths are combined using a dichroic beamsplitter (Semrock FF505-SDi01 short-pass dichroic, 80 × 50 mm).

Both excitation and emission pass through a custom-designed tube lens (Supplementary Note 1, Supplementary Fig. 2) that corrects aberrations left uncorrected by the 2p-RAM objective in the visible range to achieve diffraction-limited resolution at NA 0.4 in the GCaMP-compatible emission window at 515–535 nm.

For two-photon imaging, the motorized fold mirror mentioned above was moved out of the 2p-RAM detection path so that the system was operating as designed in two-photon imaging mode. Two-photon data was analyzed using the CaImAn signal extraction package[29].

Apparatus for stimulus delivery and behavioral tracking

Visual and somatosensory stimuli were controlled via a pre-programmed pulse table generated by National Instruments DAQ cards in the experiment control PC. For whisker stimulation, an Arduino microcontroller with a motor shield and servo motor were employed to move a brush forward and backward over the animals’ whiskers at time intervals indicated by the stimulation protocol. The brush size and its proximity were chosen to stimulate all whiskers simultaneously (as opposed to stimulation of specific whiskers), and stimulation was applied contralaterally to the hemisphere being recorded by the microscope.

All rodents were head-fixed on a home-built treadmill with a rotation encoder affixed to the rear axle (Broadcom, HEDS-5540-A02) to measure the relative position of the treadmill during the recordings. Treadmill position, the microcontroller clock value, and the onset of a whisker stimulus were streamed to the control computer via a serial port connection and logged with a separate data logging script. The data logging script also read out frames from a camera (Logitech 860–000451) to capture additional animal behavior during recordings. Motion energy (Supplementary Fig. 1) for manually defined regions of interest (e.g., front paws, nose tip) were computed from the behavior videos using the Facemap Python package[34] as the magnitude of the difference between each frame and a blockwise mean frame.

Data management and signal extraction using MesoLF computational pipeline

Data was acquired from the camera onto a control workstation (Intel Xeon W-2155 CPU 3.30 GHz, 10 cores, 256 GB RAM, Windows 10) configured with two software-defined RAID-0 arrays of two PCIe flash disks each (2× Samsung 970 EVO 2 TB and 2× Sabrent Rocket 2280 4 TB, respectively) using a custom data acquisition application written in VisualC# .NET. The magnified image covers an area of ⌀40 mm on the camera, which corresponds to ~7000 × 7000 pixels. This subset of pixels can be read out at 18 fps, resulting in a raw data rate of ~1320 MB/s.

At the end of each imaging session, the raw data was transferred via 10 Gbit/s network links to a network-attached storage server (Synology RS3618xs).

The MesoLF computational pipeline was run on a multi-GPU workstation (Titan Computers) equipped with two Intel Xeon Gold 6136 3.00GHz CPUs with 12 cores each, 260 GB RAM, three nVidia TITAN V GPUs with 12 GB RAM each, a 1 TB NVMe SSD hard disk, two 1 TB SATA SSD hard disks in a RAID-0 configuration, and a 10 Gbit/s network card. Xubuntu 20.04 was used as the operating system and all data analysis was performed in MATLAB R2020a (The Mathworks).

Running the MesoLF analysis shown in Fig. 2b (7-minute recording, 18 fps) took a total of 316 CPU core-hours and 4.1 GPU-hours, as tracked using the pidstat command. This includes loading the raw data from the network-attached storage server, which accounts for approx. 20% of the total run time and can be accelerated by holding data on local SSD disks. The full analysis run was completed within 23 hours and 26 minutes.

Throughout the manuscript, traces identified as “denoised” were denoised by fitting with an autoregressive model of calcium indicator response as implemented by the CaImAn package. Normalized fluorescence change (dF) was calculated by scaling the signal to the noise level, defined as the standard deviation of the residuals left after subtracting a low-pass-filtered version of each trace from itself and subtracting a baseline fit. Due to intermittent over-estimation of the baseline level, the noise floor on un-denoised traces may occasionally appear asymmetric or clipped. This does not affect inference of calcium transients and denoised traces since it is confined to the noise floor only. Variations in the baseline levels of un-denoised traces that are incompatible with GECI transients are rejected by the CaImAn denoising model and therefore do not appear in the denoised traces.

Hybrid “temporally interleaved” 2pM–MesoLF functional ground truth recordings

To implement the “temporally interleaved” verification modality, the 2p-RAM/MesoLF instrument used for standard MesoLF recordings was modified by replacing a fold mirror that diverted 100% of fluorescence to the MesoLF detection path during the standard MesoLF recordings with a non-polarizing beamsplitter that diverted only 80% of fluorescence to the MesoLF detection path while transmitting the remainder to the standard PMT-based detection arm of the 2p-RAM multiphoton mesoscope. A custom laser system consisting of an ultrafast fiber-based pump laser (Active Fiber Systems) and parametric chirped-pulse amplifier (Class 5 Photonics) was used to produce 2p excitation pulses at 960 nm, ~160 fs pulse duration and 4.7 MHz repetition rate. Typical laser powers at the sample were ~20–50 mW, depending on depth. Point scanning 2p excitation was performed continuously and 2pM frames were acquired continuously at a raw frame rate of 143 Hz, 141 × 141 pixels, 2 μm pixel pitch, one laser pulse per pixel.

A set of digital pulse trains was generated using a data acquisition card (National Instruments PXIe-6341) connected to the experiment control workstation, to synchronize MesoLF camera frame acquisitions relative to the 2pM frame clock. A MesoLF camera frame acquisition was triggered every 14 2pM -frames, resulting in a MesoLF frame rate of 10.2 Hz. The MesoLF widefield excitation LED (Thorlabs M470L5 with DC2200 driver,

470 nm central wavelength) was gated on during every other 2pM frame. The 2p-RAM's detection PMT module was gated off during the LED-on frames to avoid overexposure of the PMT by the LED light. Thus, only every other 2pM frame contained fluorescence signal, while the PMT-off 2pM frames were discarded. Due to this gating scheme, during each MesoLF camera frame, the excitation LED was enabled only 50% of the exposure time, resulting in a decreased signal and SNR compared to standard MesoLF recordings. This fast illumination and gating scheme on a time scale faster than the desired effective frame rate was necessary because the PMT module (Hamamatsu H11706–40) did not allow a gate-off duration of more than 10 ms. The kept 2pM frames were averaged over 7 frames, resulting in an effective 10 Hz frame rate for both MesoLF and 2pM. The frames from the two modalities contained signal that had been integrated over the exact same time period of ~ 100 ms, albeit with fast, interleaved strobing of illumination/detection that was alternated every 7 ms.

The 2pM focal plane was positioned ~50 μm above the center of the MesoLF volumes by defocusing a beam expander in the 2pM excitation beam path. This axial offset of the 2pM focus was adjusted while imaging a pollen grain test sample. To determine the relative location of the smaller 2pM FOV in the much larger MesoLF FOV, a pollen grain sample was excited with scanning 2p excitation only and recorded on both the MesoLF camera and the PMT.

During all "temporally interleaved" hybrid 2pM–MesoLF verification recordings, an air puff stimulus to the face was delivered every 60 seconds and whiskers on the contra-lateral side were stimulated using a motorized brush every 60 seconds, offset by 30 s from the air puffs. Neuronal activity was recorded for 10 min at a given depth, and up to 7 depths were recorded per mouse and session. Animal behavior was recorded with a camera (Teledyne FLIR Grasshopper 3, Thorlabs MVL16M23 objective, f = 16 mm) under IR illumination, and animal motion was tracked using a rotary encoder attached to the belt treadmill. Stimuli and behavior were controlled and/or time-stamped by an Arduino microcontroller, as in the standard MesoLF experiments described above.

The MesoLF-extracted neuron locations and time traces were then classified as true positives if the centroid of their spatial filter was within 30 μm to the centroid of a ground truth neuron. The performance scores sensitivity, precision and F-score were calculated from the resulting true/false positive rates found in the MesoLF data. The set of all matched MesoLF- and ground truth neurons was then further analyzed to obtain the distributions for localization errors, temporal correlation to ground truth, and excess correlations between pairs of traces presented in Fig. 5.

To quantify MesoLF's performance in detecting individual calcium transients, human experts annotated the raw neuronal activity traces as extracted by MesoLF and those extracted from the 2pM data by the CaImAn package, marking the timepoints at which GECI transients occurred (Supplementary Fig. 9). We then classified a transient as "detected" by MesoLF if a transient marker appeared in the MesoLF data in temporal vicinity of the corresponding 2pM transient within a window of 2 seconds. The width of this window was so chosen for two reasons: First, because GCaMP6s has relatively slow kinetics

and transients often last for seconds. Second, the transient time point assignment by human experts comes with an inherent uncertainty. We thus chose a matching window long enough to avoid mis-classifications due to imperfect transient timing estimates.

Equivalent analyses were performed on the data simulated using the NAOMi package with an active neuron density of 14,000 per mm^3 (Supplementary Note 5) to yield the performance quantifications shown in Supplementary Fig. 10–11.

Hybrid “volumetric” 2pM–MesoLF functional ground truth recordings

To complement the hybrid “temporally interleaved” 2pM–MesoLF functional ground truth recordings, we conceived of a “volumetric” 2pM–MesoLF functional ground truth recording strategy for volumetric performance validation of the MesoLF computational pipeline (Supplementary Fig. 8, Supplementary Note 11–12). This approach allowed us to generate fully volumetric functional verification datasets in which MesoLF- and 2p detection at each depth were performed truly simultaneously.

The datasets were recorded on a custom hybrid 2pM–LFM microscope. The instrument was based on Scientifica Slicescope 2pM platform with a custom LFM detection arm. Two-photon excitation pulses (920 nm, 140 fs pulse duration, 80 MHz pulse rate, Coherent Chameleon) were focused into mouse cortex and scanned in planes parallel to the cranial window at a series of depths, via the Slicescope’s galvo-galvo scan path and a Nikon 16×/0.8NA objective mounted on a motorized stage that allowed for axial translation. Fluorescence from the sample was split at a 10:90 ratio between the Slicescope’s non-descanned PMT arm (emission filter: 525/50 nm, GaAsP PMT, Hamamatsu) and a custom-built LFM arm using a 10% beam sampler (Omega) inserted behind the objective. For LFM detection, fluorescence passed through the short-pass dichroic that couples the laser into the beam path, as well as a GFP emission filter. The image formed by a standard Olympus tube lens was then relayed via two 2-inch achromat lenses (f = 200 mm, Thorlabs) onto a microlens array (MLA, Okotech, custom model, size 1” square, f-number 10, 114 μm microlens pitch, quadratic grid, no gaps). The f-number of the MLA was matched to the output f-number of the microscope. The back focal plane of the MLA was relayed by a photographic macro objective (Nikon 105 mm/2.8) at unity magnification onto the sensor of an Andor Zyla 5.5 sCMOS scientific camera (2560 × 2160 px, 16 bit). To introduce an offset between the 2pM focal plane and the LFM native focal plane, the MLA and camera were translated backwards by a distance corresponding to 40 μm in sample space. The 2pM frame clock was used to trigger camera exposures. A FOV of 200 × 200 μm was scanned at a frame rate of 5 Hz. 2-minute movies were recorded both in the PMT and the LFM camera channel at 13 depths in steps of 25 μm, ranging from 100 to 400 μm in mouse cortex.

In the LFM raw data recorded in this way, fluorescence appears to be emanating from an axial plane offset 40 μm from the axial center of the LFM volumetric field of view (due to the mentioned displacement of LFM camera and MLA backwards from the rear focal plane of the microscope).

To combine these single-plane hybrid 2pM–MesoLF recordings into volumetric functional datasets, we exploited the 3D nature of LFM acquisition and computationally shifted

the axial location of the fluorescent source plane in the LFM raw data via a simple transformation known as refocusing[35] (Supplementary Note 11). With the a-priori knowledge that all light in the LFM raw data came from a single axial plane of known depth with respect to the native focal plane, this transformation is unambiguous, relies only on elementary properties of LFM imaging and treats ballistic and scattered light in an unbiased manner. This approach allowed us to refocus and add 8 single-plane recordings such that they result in a single dataset that contains fluorescence emanating from throughout the entire LFM volumetric FOV of 200 μm axially. We built such volumetric LFM movies for two depth ranges, 100–300 and 200–400 μm, for each recorded session.

The synthetic volumetric LFM functional datasets were then processed using the MesoLF pipeline. The 2pM data was analyzed plane by plane using the CaImAn package, followed by human annotation of the CaImAn results (removing false positives, adding false negatives). This resulted in the set of neuronal positions and activity time traces that was subsequently considered the ground truth.

The MesoLF-extracted neuron locations and time traces were then classified as true positives if the centroid of their spatial filter was within 30 μm to the centroid of a ground truth neuron and had a temporal correlation with the ground truth activity trace of > 0.2. The performance scores sensitivity, precision and F-scores were calculated from the resulting true/false positive rates found in the MesoLF data. The set of all matched MesoLF- and ground truth neurons was then further analyzed to obtain the distributions for localization errors, temporal correlation to ground truth, and excess correlations between pairs of traces presented in Supplementary Fig. 8 and Supplementary Note 12.

Extended Data

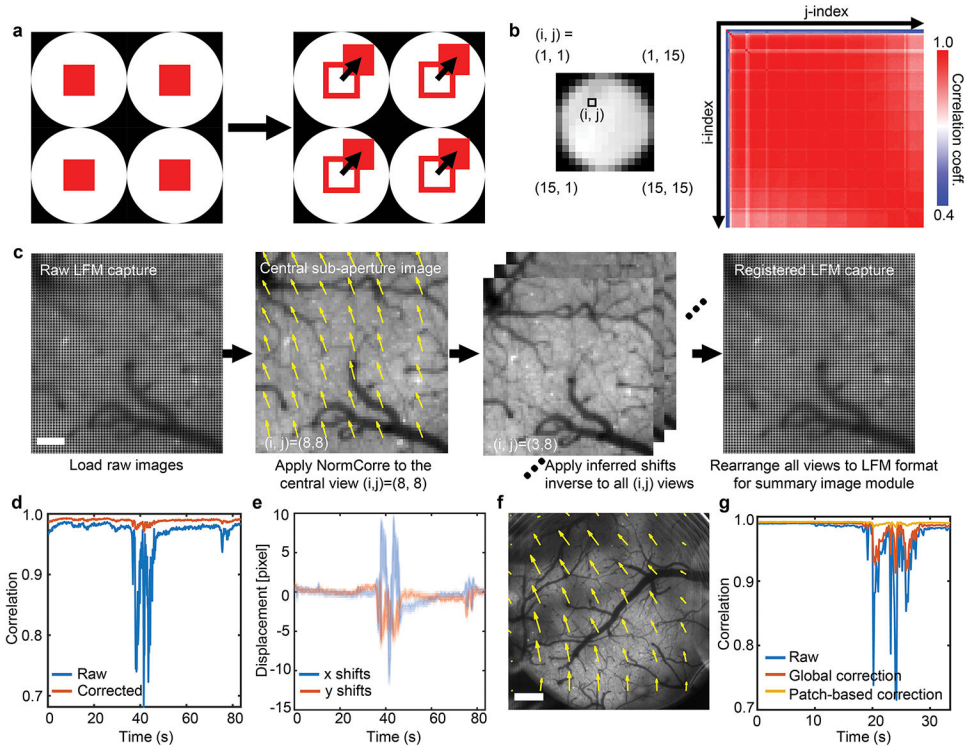

Extended Data Fig. 1. Motion correction in MesoLF.

(a) Illustrated motion patterns in LFM raw data. The lenslet aperture shadows (black areas) will not move, only patterns within those apertures (red squares), which prohibits motion correction using established algorithms without prior rearrangement of the data.

(b) Left panel: LFM image formed behind one microlens, sampled by 15 × 15 pixels. Number pairs in brackets indicate pixel coordinates (i,j). Right panel: Correlation matrix for motion vectors extracted from all 15 × 15 sub-aperture images. Sub-aperture image (i,j) consists of all pixels with coordinates (i,j) relative to the nearest microlens. Consistently high values of correlation across all pairs (i,j) indicate that all sub-aperture images experience similar motion vectors, justifying the use of the same motion correcting transformation across all sub-aperture images.

(c) Illustration of the motion correction pipeline in MesoLF. See Supplementary Note 2 for narration. Scale bar: 100 μm

(d) Correlation coefficients between successive frames of the central sub-aperture image in an LFM recording of mouse cortical calcium activity, pre- and post-motion correction (blue and red traces, respectively), for a patch size of 660 × 690 μm.

(e) Magnitude of sample motion along lateral axes (x and y, blue and red solid traces, respectively) versus time, for same recording as (d), as extracted using the MesoLF motion correction algorithm. Solid line indicates mean; shaded area indicates SD of motion in different patches across the field of view. Data identical to Fig. 4b, reproduced here for convenience.

(f) Illustration of motion vectors (arrow size indicates magnitude of motion) for different patches across the 4-mm MesoLF FOV. Scale bar: 500 μm

(g) Correlation coefficients between successive frames of the central sub-aperture movie from the whole MesoLF FOV before motion correction (blue), after global correction (red), and after patch-based correction (yellow).

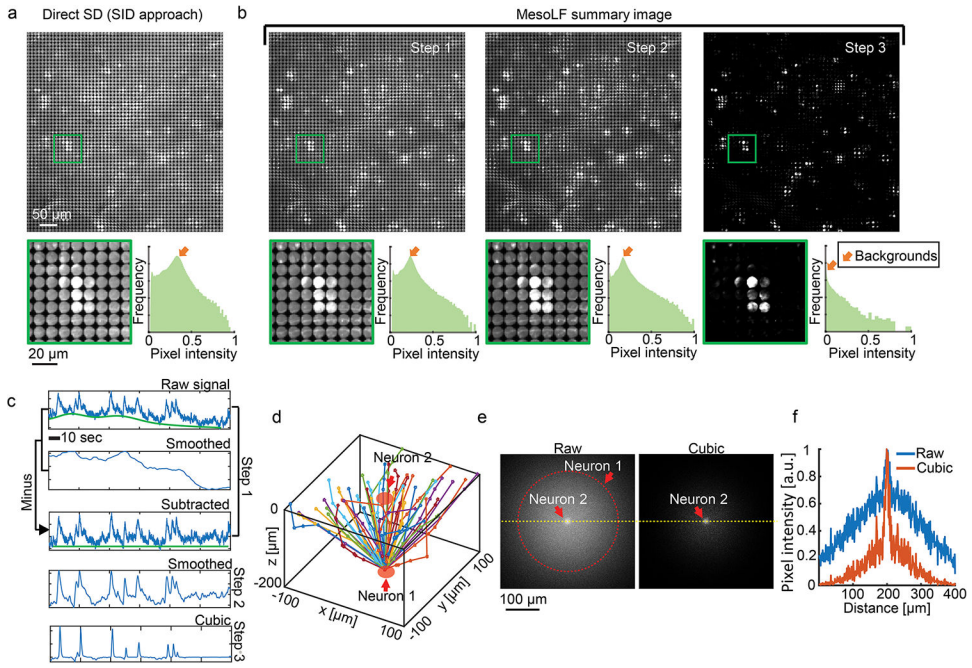

Extended Data Fig. 2. Temporal summary image generation.

(a) Top panel: Standard deviation (SD) image along time calculated directly from uncorrected raw data. Bottom left panel: Zoom into area indicated by green box. Bottom right panel: Intensity histogram of SD image shown in top panel. Orange arrow indicates the mean value of the background in the SD image.

(b) Illustration of the effect of the three preprocessing steps used in MesoLF onto the standard deviation image: In the first step, a large-window smoothed version of the data is subtracted from the raw data to flatten the baselines. In the second step, a small-window smoothing operation is applied in addition, to reduce high-frequency noise in the SD image. In the third step, the smoothed data is taken to the third power to enhance contrast. Panels in bottom row are analogous to bottom panels in (a).

(c) Illustration of the effects of the three preprocessing steps in the MesoLF pipeline onto the timeseries of a single pixel in a calcium activity recording

(d) Examples of simulated photon trajectories obtained from Monte-Carlo simulation of two neurons separated by 200 µm along the z axis. The focal plane for data shown in (e)-(f) is chosen to be the x-y plane containing neuron 2.

(e) Intensity in focal plane obtained from Monte-Carlo simulation as in (e). Left panel: raw intensity. Right panel: Third power of left panel

(f) Intensity profile along the dashed yellow line in the two panels shown in (f).

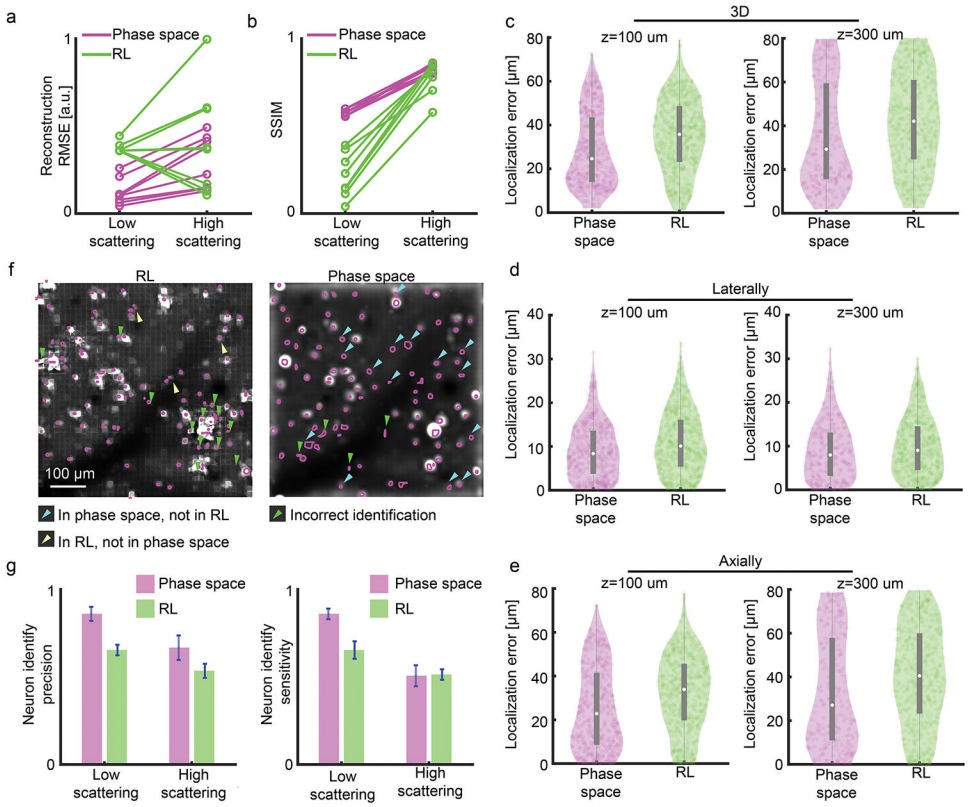

Extended Data Fig. 3. Statistical comparison of pixel-space Richardson-Lucy and MesoLF phase space reconstructions.

(a) Comparison of root-mean-square error (RMSE) between ground truth and reconstructions obtained using pixel-space Richardson-Lucy (RL) reconstruction and MesoLF phase space reconstructions (Supplementary Note 4), for the low- and high scattering scenarios. n = 8 data points represent runs with different simulated raw data.

(b) Comparison of the structure similarity index (SSIM) values between ground truth and reconstructions, same underlying data as in (a), n = 8 different simulation runs

(c) Violin plots of the 3D localization errors between ground truth neurons and neurons extracted from phase space (magenta) and RL (green) reconstructions, in the low and high scattering scenarios (depths 100 µm and 300 µm, respectively). White circle: median. Thick grey vertical line: Interquartile range. Thin vertical lines: Upper and lower proximal values. Solid disks: data points. Transparent violin-shaped area: Kernel density estimate of data distribution. n = 580 for phase space, n = 427 for RL, z = 100 µm; n = 541 for phase space, n = 258 for RL, z = 300 µm.

(d) As in (c), but lateral localization error only. Violin plot elements as in (c). n = 580 for phase space, n = 427 for RL, z = 100 µm; n = 541 for phase space, n = 258 for RL, z = 300 µm

(e) As in (c), but axial localization errors only. Violin plot elements as in (c). n = 580 for phase space, n = 427 for RL, z = 100 µm; n = 541 for phase space, n = 258 for RL, z = 300 µm

(f) Example plane from reconstructions obtained using RL (left panel) and MesoLF phase space reconstruction (right panel). Magenta circles in the left panel show the segmentation

result obtained using the segmentation approach in the SID package (Nöbauer et al., Nat. Methods 14, 2017). Magenta circles in the right panel are segments obtained using MesoLF segmentation. Blue arrows mark the true neurons that appear only in the phase space reconstruction. Yellow arrows mark the true neurons that only appear in the RL reconstruction. Green arrows mark false neuron segments found in reconstructions using both methods.

(g) Comparison of segmentation precision and sensitivity values obtained using phase space (magenta) and RL (green) reconstructions, for the low and high scattering scenarios. Central measure: Mean. Error bars: SD. Black circles: n = 5 different simulation runs.

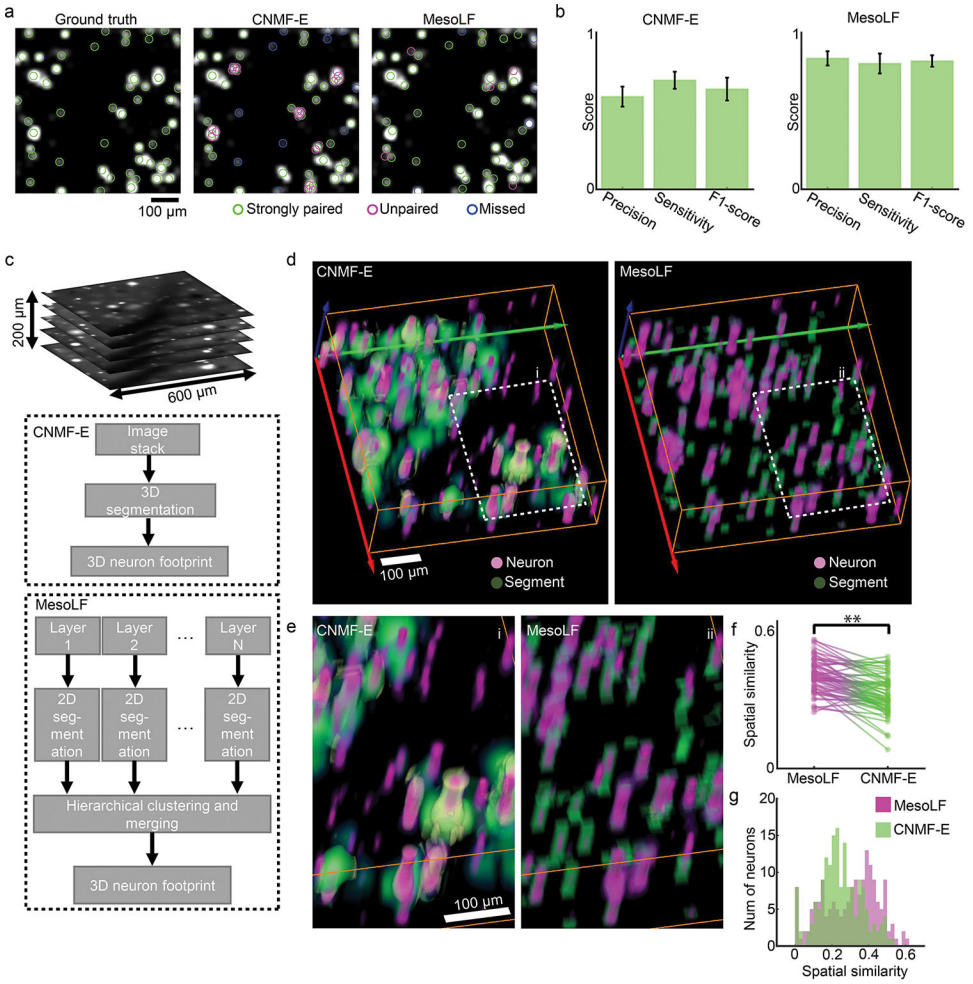

Extended Data Fig. 4. Neuron segmentation performance.

(a) Comparison of segmentation performance of MesoLF versus CNMF-E (template matching and shape-based selection steps) in a 2D slice from a MesoLF recording in mouse cortex, depth 100 µm. Green circles: segments that strongly match with the ground truth. Blue circles: segments that only appear in the ground truth. Magenta circles: segments that are not consistent with ground truth.

(b) Comparison of precision, sensitivity, and F1-scores for neuron detection performance in CNMF-E (template matching and shape-based selection steps) and MesoLF segmentation.

Same data as in main Fig. 3h, reproduced here for convenience. Height of bars: Mean. Error bars: SD. Black circles: n = 5 simulation runs.

(c) Top panel: Illustration of 3D volume containing neurons and exhibiting scattering, as used for volumetric segmentation comparisons in remainder of figure. Schematic illustration of segmentation pipelines in CNMF-E (middle box) and MesoLF (bottom box).

(d) 3D rendering of segmentation results from CNMF-E (left) and MesoLF (right). Magenta: Ground truth neurons, green: segments.

(e) Zooms into areas indicated by dashed rectangles in (d).

(f) Comparison of the spatial similarity index of neurons paired between ground truth and output of CNMF-E (template matching and shape-based selection steps) versus MesoLF segmentation. p = 2.0e-9, paired one-sided Wilcoxon signed rank test. n = 63 neuron pairs. ** $p < 0.01$.

(g) Histogram of spatial similarity indices of segmented neurons compared to ground truth by both methods (same data as in (f)).

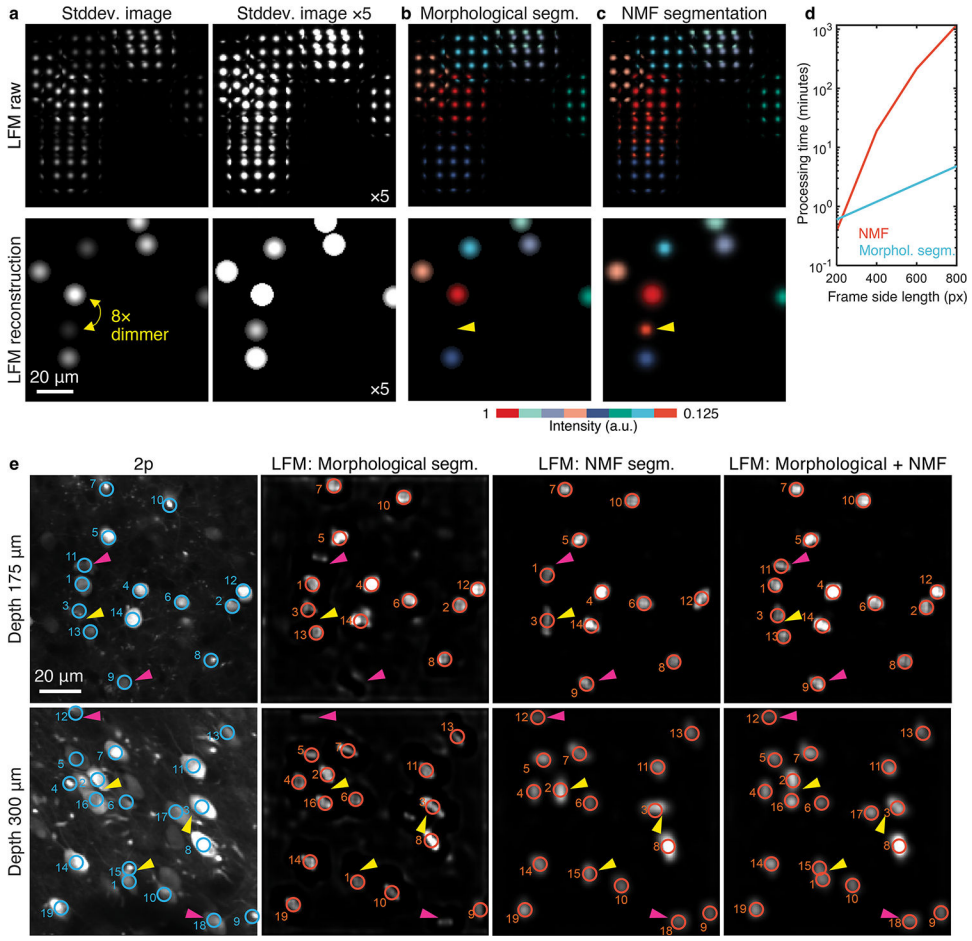

Extended Data Fig. 5. Enhancing detection of weakly active neurons by combining morphological segmentation with NMF.

(a) Left column: Standard deviation (SD) images of simulated LFM movie containing temporally active neurons (top) and a single plane from reconstructed SD image (bottom). The brightness values (i.e., magnitude of SD of their activity) of neurons in the SD image

is chosen such that dimmest (least active) neuron is 8 times dimmer than the brightest (most active) one (indicated by yellow double arrow). Right column: Same as left column with brightness scaled 5× for clarity.

(b) Result of morphological segmentation (Supplementary Note 6) applied to simulated data shown in (a). Individual segments highlighted in different colors. Dimmest neuron (yellow arow) is not segmented successfully and missed.

(c) Result of NMF-based segmentation (Supplementary Note 7) applied to simulated data shown in (a). Individual segments highlighted in different colors. Dimmest neuron (yellow arow) is segmented successfully and detected.

(d) Runtime comparison of NMF- and morphology-based methods. The morphology-based method is faster by orders of magnitude as the input frame side length increases.

(e) Comparison between “ground truth” CaImAn-based segmentation of two-photon microscopy data (first column) to segmentation results obtained from morphological segmentation (second column), NMF-based segmentation (third column), and the combination of both (fourth column), for two different depths (170 µm, top row. 300 µm, bottom row). The purely morphological segmentation approach performs well in segmenting neurons but sometimes misses very dim neurons in the temporal summary image (highlighted with pink arrows). The NMF-based approach on the other hand tends to detect dim neurons more reliably (pink arrows) but comes with the risk of mis-segmenting close-by neurons and assigning them to one component only (yellow arrows). Combining both methods lead to the best results but incurs the largest computational cost of the three approaches since NMF has to be run on the full frames. It should therefore only be used if maximal detection sensitivity is required or if only a subset of the full MesoLF FOV is being used.

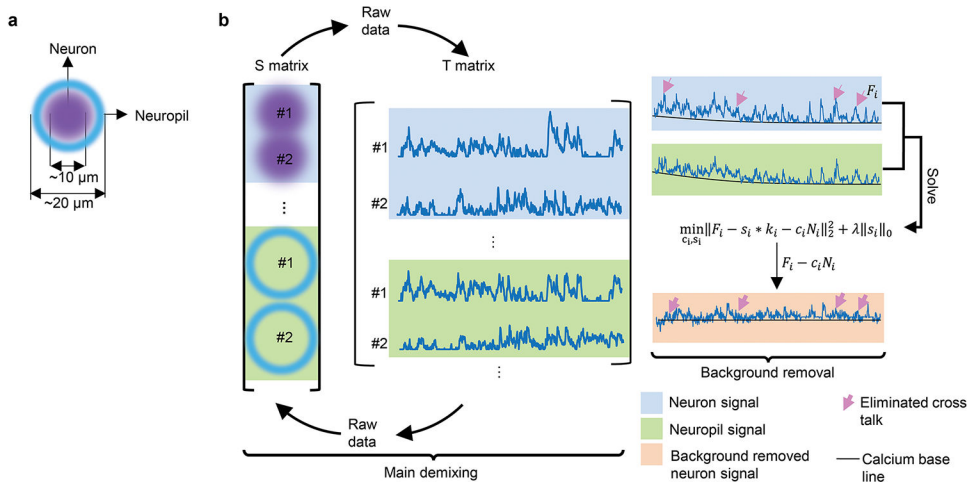

Extended Data Fig. 6. Core-shell demixing.

(a) Illustration of core-shell model used for demixing neuronal signals from local background.

(b) Left part: Illustration of the MesoLF main demixing stage, during which the spatial footprints and temporal traces of both core (neuron) and shell (background, neuropil) components are updated alternatingly and iteratively. Right part: After the main demixing

step, a second optimization is run to infer the amplitude mixing coefficient, which subsequently allows to subtract shell contaminations from the core region.

Supplementary Material

Refer to Web version on PubMed Central for supplementary material.

ACKNOWLEDGMENTS

We thank Peer Strogies and James Petrillo at the Rockefeller University's Precision Instrumentation Technology (PIT) for fabrication of mechanical components, David Hillebrand (Rockefeller University) for sharing reagents, Juro Gottweis (Google Inc.) for an initial GPU-implementation approach of a light-field-related operation, and Francisca Martínez-Traub (Rockefeller University) for surgeries. Research reported in this publication was supported by the National Institute of Neurological Disorders and Stroke of the National Institutes of Health under award numbers 5U01NS103488 (A.V.), 1RF1NS110501 (A.V.), 1RF1NS113251 (A.V.), the National Science Foundation under award number NSF-DBI-1707408 (A.V.) and the Kavli Foundation through the Kavli Neural System Institute (A.V.), in particular through a Kavli Neural Systems Institute postdoctoral fellowship (T.N.).

DATA AVAILABILITY

A comprehensive demo dataset, complete expected outputs from the demo, as well as all required auxiliary files (pretrained classifier models, pre-computed point spread function) are available for download[22]. A demo script is contained in Supplementary Software 1. The demo script automatically downloads the demo data. Due to the very large and diversely structured data, not all data are currently available in annotated format, but can be obtained from the corresponding author upon reasonable request.

REFERENCES

1. Broussard GJ, Liang Y, Fridman M, Unger EK, Meng G, Xiao X, Ji N, Petreanu L & Tian L In vivo measurement of afferent activity with axon-specific calcium imaging. Nat. Neurosci. 21, 1272–1280 (2018). [PubMed: 30127424]
2. Dana H, Mohar B, Sun Y, Narayan S, Gordus A, Hasseman JP, Tsegaye G, Holt GT, Hu A, Walpita D, Patel R, Macklin JJ, Bargmann CI, Ahrens MB, Schreiter ER, Jayaraman V, Looger LL, Svoboda K & Kim DS Sensitive red protein calcium indicators for imaging neural activity. eLife 5, e12727 (2020).
3. Dana H, Sun Y, Mohar B, Hulse BK, Kerlin AM, Hasseman JP, Tsegaye G, Tsang A, Wong A, Patel R, Macklin JJ, Chen Y, Konnerth A, Jayaraman V, Looger LL, Schreiter ER, Svoboda K & Kim DS High-performance calcium sensors for imaging activity in neuronal populations and microcompartments. Nat. Methods 16, 649 (2019). [PubMed: 31209382]
4. Demas J, Manley J, Tejera F, Barber K, Kim H, Traub FM, Chen B & Vaziri A High-speed, cortex-wide volumetric recording of neuroactivity at cellular resolution using light beads microscopy. Nat. Methods 18, 1103–1111 (2021). [PubMed: 34462592]
5. Levoy M, Ng R, Adams A, Footer M & Horowitz M Light field microscopy. ACM Trans. Graph. 25, 924 (2006).
6. Broxton M, Grosenick L, Yang S, Cohen N, Andalman A, Deisseroth K & Levoy M Wave optics theory and 3-D deconvolution for the light field microscope. Opt. Express 21, 25418–25439 (2013). [PubMed: 24150383]
7. Prevedel R, Yoon Y-G, Hoffmann M, Pak N, Wetzstein G, Kato S, Schrödel T, Raskar R, Zimmer M, Boyden ES & Vaziri A Simultaneous whole-animal 3D imaging of neuronal activity using light-field microscopy. Nat. Methods 11, 727–730 (2014). [PubMed: 24836920]
8. Pégard NC, Liu H-Y, Antipa N, Gerlock M, Adesnik H & Waller L Compressive light-field microscopy for 3D neural activity recording. Optica 3, 517 (2016).

9. Cong L, Wang Z, Chai Y, Hang W, Shang C, Yang W, Bai L, Du J, Wang K & Wen Q Rapid whole brain imaging of neural activity in freely behaving larval zebrafish (Danio rerio). eLife 6, e28158 (2017). [PubMed: 28930070]
10. Scrofani G, Sola-Pikabea J, Llavador A, Sanchez-Ortiga E, Barreiro JC, Saavedra G, Garcia-Sucerquia J & Martínez-Corral M FIMic: design for ultimate 3D-integral microscopy of in-vivo biological samples. Biomed. Opt. Express 9, 335 (2018). [PubMed: 29359107]
11. Lu Z, Wu J, Qiao H, Zhou Y, Yan T, Zhou Z, Zhang X, Fan J & Dai Q Phase-space deconvolution for light field microscopy. Opt. Express 27, 18131–18145 (2019). [PubMed: 31252761]
12. Chen Y, Xiong B, Xue Y, Jin X, Jin X, Greene J, Tian L & Tian L Design of a high-resolution light field miniscope for volumetric imaging in scattering tissue. Biomed. Opt. Express 11, 1662–1678 (2020). [PubMed: 32206434]
13. Adams JK, Boominathan V, Avants BW, Vercosa DG, Ye F, Baraniuk RG, Robinson JT & Veeraraghavan A Single-frame 3D fluorescence microscopy with ultraminiature lensless FlatScope. Sci. Adv. 3, e1701548 (2017). [PubMed: 29226243]
14. Fan J, Suo J, Wu J, Xie H, Shen Y, Chen F, Wang G, Cao L, Jin G, He Q, Li T, Luan G, Kong L, Zheng Z & Dai Q Video-rate imaging of biological dynamics at centimetre scale and micrometre resolution. Nat. Photonics 13, 809–816 (2019).
15. Xue Y, Davison IG, Boas DA & Tian L Single-shot 3D wide-field fluorescence imaging with a Computational Miniature Mesoscope. Sci. Adv. 6, eabb7508 (2020). [PubMed: 33087364]
16. Xiao S, Gritton H, Tseng H-A, Zemel D, Han X, Han X, Han X, Mertz J, Mertz J & Mertz J High-contrast multifocus microscopy with a single camera and z-splitter prism. Optica 7, 1477–1486 (2020). [PubMed: 34532564]
17. Kauvar IV, Machado TA, Yuen E, Kochalka J, Choi M, Allen WE, Wetzstein G & Deisseroth K Cortical Observation by Synchronous Multifocal Optical Sampling Reveals Widespread Population Encoding of Actions. Neuron 107, 351–367.e19 (2020). [PubMed: 32433908]
18. Nöbauer T, Skocek O, Pernía-Andrade AJ, Weilguny L, Martínez Traub F, Molodtsov MI & Vaziri A Video rate volumetric Ca2+ imaging across cortex using seeded iterative demixing (SID) microscopy. Nat. Methods 14, 811–818 (2017). [PubMed: 28650477]
19. Skocek O, Nöbauer T, Weilguny L, Martínez Traub F, Xia CN, Molodtsov MI, Grama A, Yamagata M, Aharoni D, Cox DD, Golshani P & Vaziri A High-speed volumetric imaging of neuronal activity in freely moving rodents. Nat. Methods 15, 429–432 (2018). [PubMed: 29736000]
20. Sofroniew NJ, Flickinger D, King J & Svoboda K A large field of view two-photon mesoscope with subcellular resolution for in vivo imaging. eLife 5, e14472 (2016). [PubMed: 27300105]
21. Bentley J & Olson C Field guide to lens design. (SPIE, 2012).
22. Nöbauer T, Zhang Y, Kim H & Vaziri A MesoLF demo data and auxiliary files. (2022). doi:10.5281/zenodo.7306113
23. Shemesh OA, Linghu C, Piatkevich KD, Goodwin D, Celiker OT, Gritton HJ, Romano MF, Gao R, Yu C.-C. (Jay), Tseng H-A, Bensussen S, Narayan S, Yang C-T, Freifeld L, Siciliano CA, Gupta I, Wang J, Pak N, Yoon Y-G, Ullmann JFP, Guner-Ataman B, Noamany H, Sheinkopf ZR, Park WM, Asano S, Keating AE, Trimmer JS, Reimer J, Tolias AS, Bear MF, Tye KM, Han X, Ahrens MB & Boyden ES Precision Calcium Imaging of Dense Neural Populations via a Cell-Body-Targeted Calcium Indicator. Neuron 107, 470–486.e11 (2020). [PubMed: 32592656]
24. Mukamel EA, Nimmerjahn A & Schnitzer MJ Automated Analysis of Cellular Signals from Large-Scale Calcium Imaging Data. Neuron 63, 747–760 (2009). [PubMed: 19778505]
25. Zhou P, Resendez SL, Rodriguez-Romaguera J, Jimenez JC, Neufeld SQ, Giovannucci A, Friedrich J, Pnevmatikakis EA, Stuber GD, Hen R, Kheirbek MA, Sabatini BL, Kass RE & Paninski L Efficient and accurate extraction of in vivo calcium signals from microendoscopic video data. eLife 7, e28728 (2018). [PubMed: 29469809]
26. Song A, Gauthier JL, Pillow JW, Tank DW & Charles AS Neural anatomy and optical microscopy (NAOMi) simulation for evaluating calcium imaging methods. J. Neurosci. Methods 358, 109173 (2021). [PubMed: 33839190]
27. Tibshirani R Regression Shrinkage and Selection Via the Lasso. J. R. Stat. Soc. Ser. B Methodol. 58, 267–288 (1996).

28. Azzopardi G, Strisciuglio N, Vento M & Petkov N Trainable COSFIRE filters for vessel delineation with application to retinal images. Med. Image Anal. 19, 46–57 (2015). [PubMed: 25240643]

29. Giovannucci A, Friedrich J, Gunn P, Kalfon J, Brown BL, Koay SA, Taxidis J, Najafi F, Gauthier JL, Zhou P, Khakh BS, Tank DW, Chklovskii DB & Pnevmatikakis EA CaImAn an open source tool for scalable calcium imaging data analysis. eLife 8, e38173 (2019). [PubMed: 30652683]

30. Pachitariu M, Stringer C, Dipoppa M, Schröder S, Rossi LF, Dalgleish H, Carandini M & Harris KD Suite2p: beyond 10,000 neurons with standard two-photon microscopy. bioRxiv 061507 (2017). doi:10.1101/061507

31. Soltanian-Zadeh S, Sahingur K, Blau S, Gong Y & Farsiu S Fast and robust active neuron segmentation in two-photon calcium imaging using spatiotemporal deep learning. Proc. Natl. Acad. Sci. 201812995 (2019). doi:10.1073/pnas.1812995116

32. Bando Y, Sakamoto M, Kim S, Ayzenshtat I & Yuste R Comparative Evaluation of Genetically Encoded Voltage Indicators. Cell Rep. 26, 802–813.e4 (2019). [PubMed: 30650368]

33. Knöpfel T & Song C Optical voltage imaging in neurons: moving from technology development to practical tool. Nat. Rev. Neurosci. 20, 719–727 (2019). [PubMed: 31705060]

METHODS-ONLY REFERENCES

34. Stringer C, Pachitariu M, Steinmetz N, Reddy CB, Carandini M & Harris KD Spontaneous behaviors drive multidimensional, brainwide activity. Science 364, (2019).

35. Ng R Digital Light Field Photography. (PhD thesis, Stanford University, 2006). at https://stanford.edu/class/ee367/reading/Ren%20Ng-thesis%20Lytro.pdf

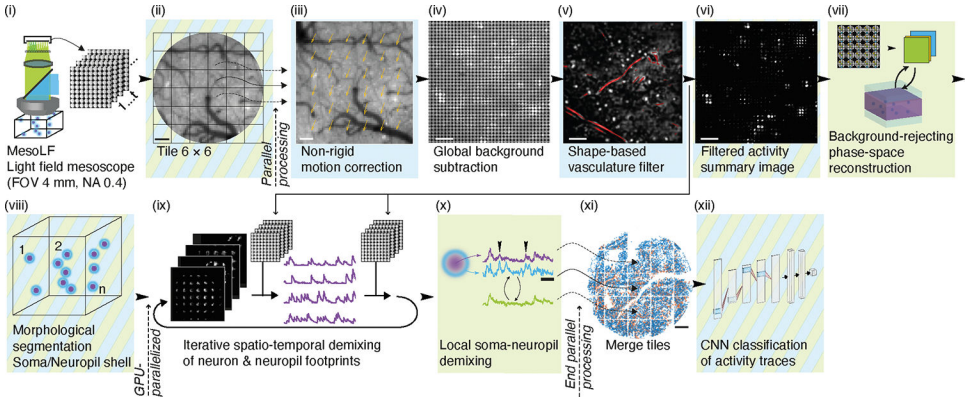

Figure 1 |. Mesoscopic Light Field (MesoLF) computational pipeline.

Overview of MesoLF computational pipeline. Fluorescence from the sample is imaged through custom-designed optics (FOV ⌀ 4 mm, NA 0.4) in an LFM detection arm onto a CMOS camera (~50M pixels per frame, 6 μm pixel size, 18 fps) and streamed to a flash disk array (i). Frames are tiled into 6 × 6 patches and processed in parallel on a multi-GPU workstation (ii). Non-rigid motion correction (iii) and background subtraction (iv). Blood vessels are detected and masked (v). Temporal filtering removes low- and high-frequency noise. A temporal activity summary image is computed to highlight temporally active pixels (vi). From the summary image, a 3D volume containing the active neurons is reconstructed using an artifact-free phase-space reconstruction algorithm that performs background-“peeling”, i.e., estimation and subtraction of temporally variable background above and below the target volume (vii). A custom morphological segmentation algorithm segments active neurons in the reconstructed volume (viii). For each candidate neuron and its local surrounding shell, a mask is generated that represents its anticipated spatial footprint in the LFM camera data. In an iterative optimization, these spatial footprints and the corresponding activity time series are updated, thus demixing the neuronal activity signals present in the recording (ix). The input data that is being demixed in this step is the background-subtracted and vasculature-filtered data that is the output of step (v), as indicated by an arrow. The resulting neuron- and background-shell signals are further demixed by solving an optimization problem that seeks to reduce crosstalk between neurons and the local background shell components (x). Neuron positions and activity signals from each patch are merged (xi) and classified into high- and low-quality traces by a neuronal network (xii). Green boxes and hatches indicate modules for improving general signal extraction quality. Blue boxes and hatches indicate those designed to mitigate signal contaminants and other issues associated with multi-millimeter-scale imaging in mammalian brains. Scale bars: (ii), (iii), (xi): 500 μm. (iv)-(vi): 50 μm. (x) 10 s.

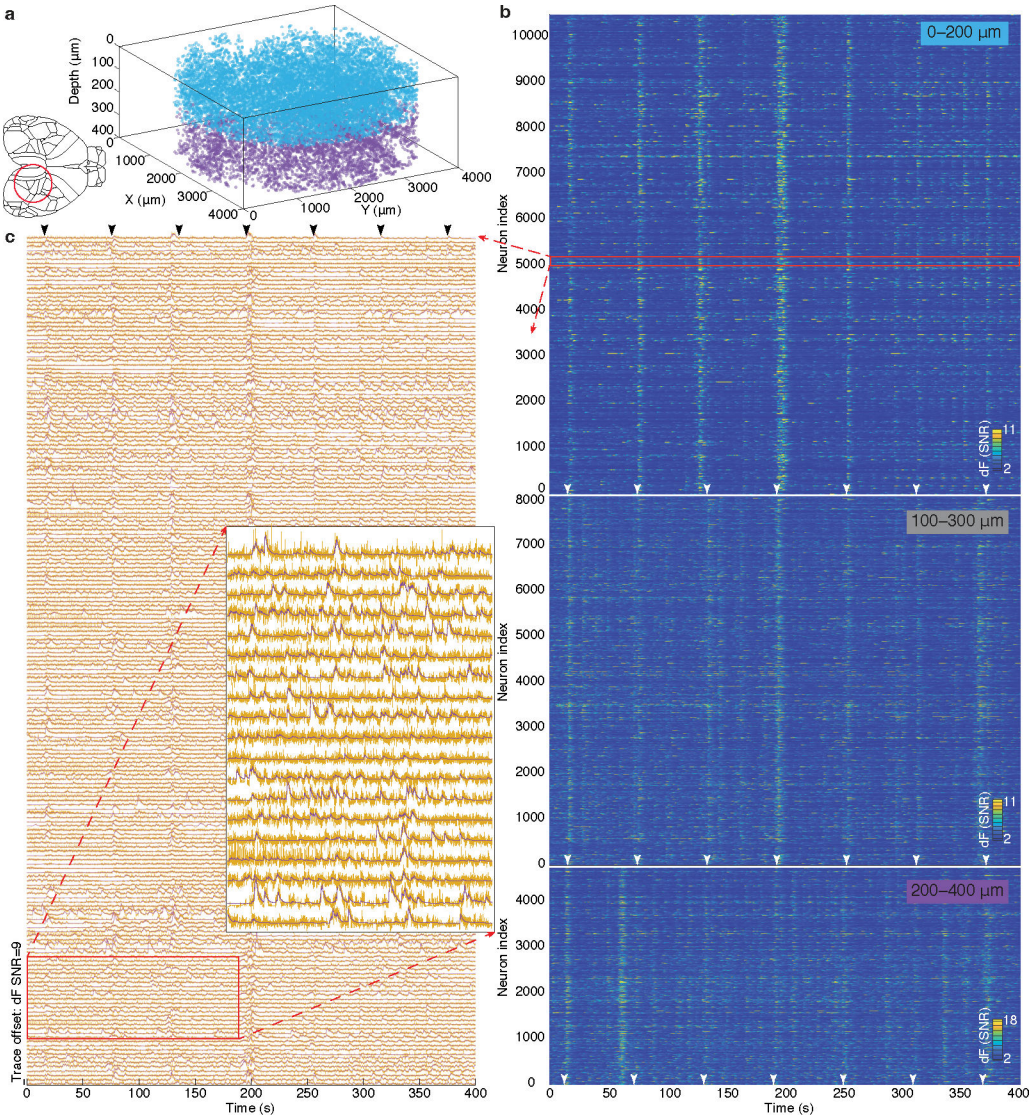

Figure 2 |. MesoLF calcium imaging in the scattering rodent cortex.

(a) 3D rendering of single neuron positions within an overall volume of ⌀ 4 mm × 400 µm obtained by MesoLF from two subsequent 405-second recordings at 18 volumes per second in mouse cortex. Neuron positions from two sequential recordings of different depth ranges are shown together. Colors indicate recording depth range: blue, 0–200 µm; purple, 200–400 µm. Inset: Approximate position of the imaged ⌀4 mm FOV (red circle) superimposed onto an outlined top projection view of the Allen Mouse Brain Reference Atlas (showing cortex only). Cortical areas contained in the imaged FOV include the posterior parietal, primary somatosensory, primary visual, anteromedial visual, and retrosplenial cortical area.

(b) Heat maps of denoised temporal signals extracted from three 405-second recordings at 18 Hz in mouse cortex at three different depth ranges, sorted by depth (lower index is lower depth). Top panel, 10,580 neurons detected in depth range 0–200 µm. Middle panel: 8,076 neurons found in depth range 100–300 µm. Bottom panel: 4,746 neurons found in 200–400 µm depth range. Top and bottom panels correspond to neuron positions shown in **a**

in blue and violet, respectively. Traces shown are those retained by the CNN trace classifier in "sensitive" mode, of which 1817 (0–200 μm), 1112 (100–300 μm) and 709 (200–400 μm) were classified as high quality and the remainder as intermediate quality. The red rectangle indicates the zoom-in region shown in **c**. White arrows indicate whisker stimulus onset. Color scale: Fluorescence change (dF) normalized to noise SD. Color scales clipped to 15th and 99.9th percentile of each panel for clarity.

(c) Stacked neuronal activity traces for region indicated by red rectangle in **b**. Traces are normalized to noise SD as in **b** and baseline-subtracted (may cause visual clipping of noise floor). Spacing of traces corresponds to 9 SD of the noise. Yellow lines: un-denoised output of MesoLF pipeline. Violet lines: Denoising fit. Black arrows indicate whisker stimulus onset. Inset is zoom into area indicated by red rectangle. Data in **(a)–(c)** representative of 31 recordings from 6 mice.

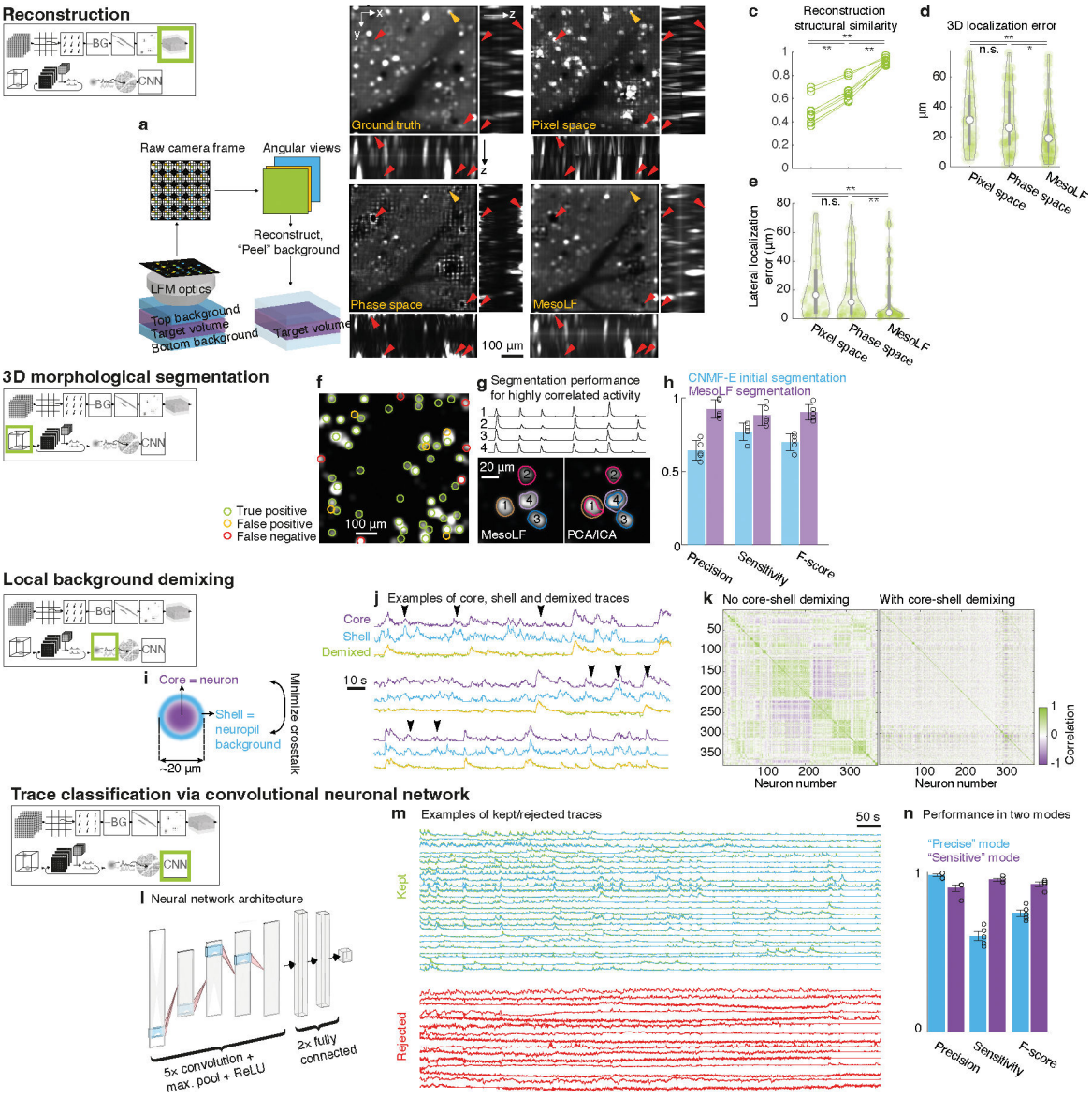

Figure 3 |. Performance and verification of the individual modules of the MesoLF computational pipeline.

(a) Illustration of MesoLF light field phase space reconstruction with background peeling. **(b)** Comparison of volumetric light field reconstruction methods and ground truth. Top left: simulated ground truth volume containing neurons, blood vessels, and neuropil. Top right: Volumetric reconstruction of simulated LFM raw data using Richardson-Lucy deconvolution (Pixel space). Bottom left: Reconstruction using phase space deconvolution without background peeling (Phase space). Bottom right: Reconstruction using phase space deconvolution with background peeling (MesoLF). Red arrows: positions where artefacts are present in other methods but absent in MesoLF reconstruction. Yellow arrows: position where a ground truth neuron was falsely suppressed in MesoLF. All panels: large image is x-y slice at z = 60 µm. Smaller images are maximum intensity projections of the reconstructed

volume along the x and y axes, respectively. Simulated depth of center of volume: 60 μm. Size of volumes: 600 × 600 × 200 μm^3, depth range 0–200 μm

(c) Structural similarity index between the simulated ground truth volume and the three different classes of reconstructed volumes shown in **b**, quantifying quality of reconstruction. n = 9 sets of reconstructions. Paired two-sided Wilcoxon signed rank test for equal median. p = 0.004 (pixel space vs. phase space), 0.004 (pixel space vs. MesoLF), 0.004 (phase space vs. MesoLF). ** $p < 0.01$.

(d) Violin plot of 3D localization error, defined as minimum 3D distance between neurons in simulated ground truth and neurons found in the three different reconstructions shown in **b**. White circle: median. Thick grey vertical line: Interquartile range. Thin vertical lines: Upper and lower proximal values. Transparent blue disks: data points. Transparent violin-shaped area: Kernel density estimate of data distribution. n = 60, 79, 94 data points, respectively. Two-sided Wilcoxon rank sum test for equal medians, p = 0.567 (pixel space vs. phase space), 0.003 (pixel space vs. MesoLF), 0.019 (phase space vs. MesoLF). n.s., not significant. * $p < 0.05$, ** $p < 0.01$.

(e) Violin plot of lateral localization error, defined as minimum lateral distance between neurons in simulated ground truth and neurons found in the three different reconstructions shown in b. Symbols as in **d**. n = 65, 87, 104 data points, respectively. Two-sided Wilcoxon rank sum test for equal medians, p = 0.766 (pixel space vs. phase space), 0.009 (pixel space vs. MesoLF), 0.029 (phase space vs. MesoLF). n.s., not significant. ** $p < 0.01$. Violin plot elements as in **d**.

(f) Segmentation performance in MesoLF. Background: Slice from volume reconstruction of temporal summary image, SomaGCaMP7f, mouse cortex, depth 100 μm, simulated data. Colored circles indicate MesoLF segmentation results compared to manual segmentation.

(g) Comparison of MesoLF segmentation performance versus PCA/ICA-based segmentation for four simulated neurons with highly correlated temporal activities (activity traces shown above segmented images). Ground truth neurons and corresponding time traces labelled with black digits. Individual segments shown as contour lines with different colors. Note the overlapping and under-segmented output from PCA/ICA.

(h) Overall neuron detection scores for the MesoLF morphological segmentation compared to the CNMF-E initial segmentation phase (template matching and shape-based selection steps) (simulated, SomaGCaMP7f, mouse cortex, depth 100 μm). Height of bars: Mean. Error bars: SD. Black circles: n = 5 simulation runs.

(i) Illustration of core-shell geometry for demixing neuropil activity from soma signals. Signals from segmented regions in **f** (cores, neurons) and a Gaussian shell region (extending from ~10 to ~20 μm diameter) surrounding the cores (background shell, neuropil) are identified and demixed.

(j) Sets of representative example traces for core, shell, and demixing result, taken from a recording in mouse cortex at depths 200–400 μm. Arrows indicate crosstalk between shell and core that is removed in the demixed traces. Experimental data from SomaGCaMP7f-labelled mouse cortex, depth 100 μm.

(k) Matrices of Pearson correlation coefficients between 400 pairs of neuronal activity traces extracted from a MesoLF recording in mouse cortex, before and after core-shell demixing. Average absolute correlation between signal pairs is reduced by 37% in MesoLF.

(l) Illustration of convolutional neural network (CNN) architecture used for classification of candidate neural activity traces

(m) Representative examples of 25 kept and 10 rejected traces by CNN. Experimental data, SomaGCaMP7f, mouse cortex, various depths.

(n) Classification performance of two differently trained CNNs, one optimized for prioritizing precision ("precise mode", blue bars) and one for prioritizing sensitivity ("sensitive mode", violet bars), both while maintaining an overall high F-score. The CNN in "precise" mode achieves precision 0.98 ± 0.01, sensitivity 0.60 ± 0.03, F-score 0.75 ± 0.02; CNN "sensitive" mode achieves precision 0.90 ± 0.02, sensitivity 0.96 ± 0.01, F-score 0.93 ± 0.01. Classification performance evaluated on withheld data that was not used during training. Height of bars: Mean. Error bars: SD. Black circles: n = 5 held-out datasets in each bar.

Boxed insets: Miniature representations of the pipeline schematic shown in Fig. 1, for orientation.

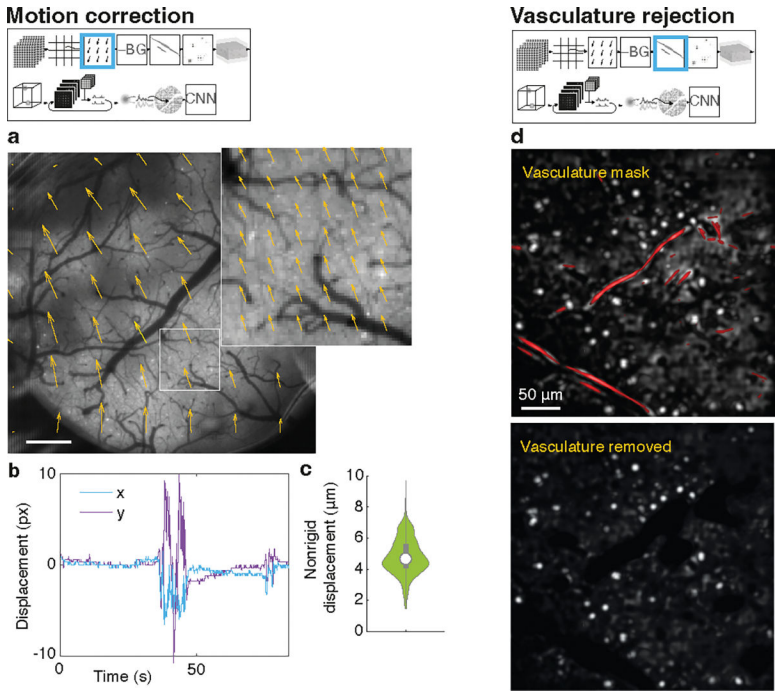

Figure 4 |. MesoLF pipeline modules mitigating contaminants at mesoscopic scale.

(a) Motion correction in MesoLF. Background is single frame from MesoLF experimental raw data, central sub-aperture image, full FOV (scale bar: 500 μm). Orange arrows: direction and magnitude (scaled for clarity, a.u.) of rigid motion correction applied to each of the 6 × 6 tiles into which the raw frame is split at the beginning of the MesoLF pipeline. Inset: Zoom into one of the tiles as indicated with white square. Width of tile: 680 μm. Orange arrows: non-rigid motion correction applied within tile. Data representative of 31 recordings from 6 mice.

(b) Example of lateral displacement (blue line: x-direction, violet line: y-direction) versus time for one of the tiles in top left panel.

(c) Violin plot of non-rigid displacements (i.e., displacements remaining after rigid motion correction). White circle: median. Thick grey vertical line: Interquartile range. Thin vertical lines: Upper and lower proximal values. Transparent blue disks: data points. Transparent violin-shaped area: Kernel density estimate of data distribution. n = 201 data points.

(d) Top: Example slice from volume reconstruction of MesoLF temporal activity summary image, with vasculature mask overlaid in red. Bottom: Same slice as in top panel, with vasculature removed. Experimental data, SomaGCaMP7f, mouse cortex, depth <50 μm. Boxed insets: Miniature representations of the pipeline schematic shown in Fig. 1, for orientation.

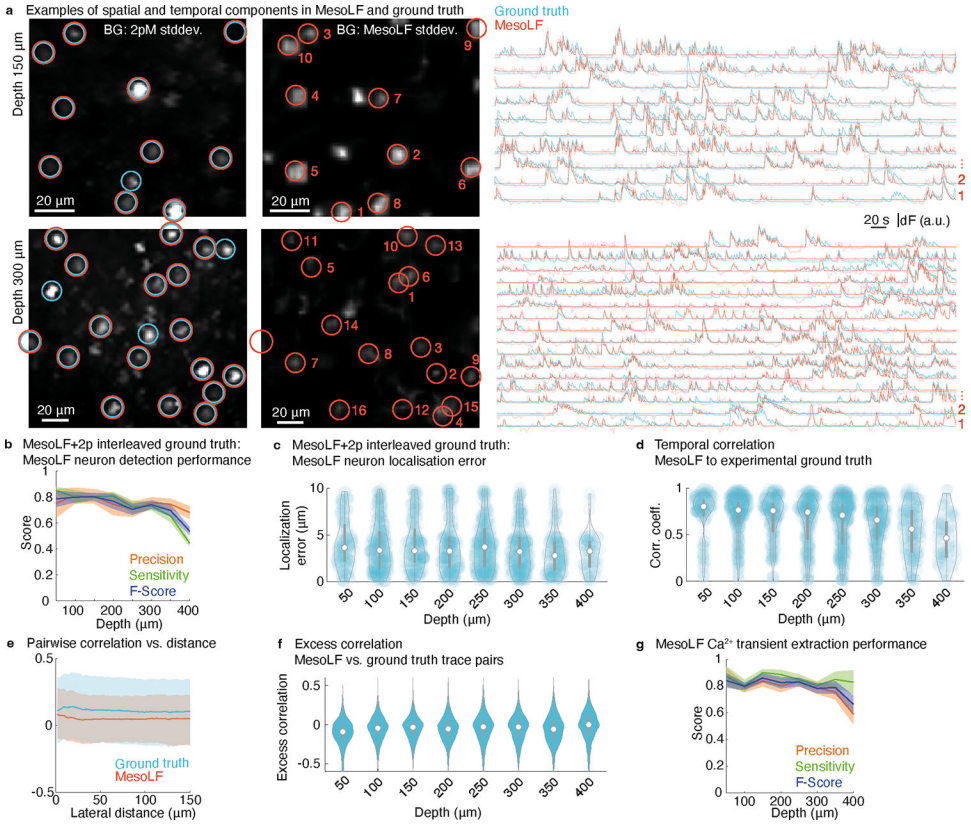

Figure 5 |. Experimental performance of full MesoLF pipeline versus quasi-simultaneously acquired functional ground truth data

"Temporally interleaved" 2pM–MesoLF functional ground truth generated by interleaving volumetric MesoLF frames and planar 2pM frames. Data in **a–g** is based on a total of 34 recordings from 3 mice.

(a) Left column: Ground truth (blue circles) and MesoLF-extracted neuron positions (red circles) overlaid on a 2pM temporal standard deviation image from "temporally interleaved" 2pM–MesoLF recording, for two different depths (top: 150 µm; bottom: 300 µm). Full 2pM FOV of 280 × 280 µm is cropped for clarity. Middle column: MesoLF-extracted neuron positions (red circles) overlaid on a slice from the reconstructed MesoLF temporal summary volume corresponding to the depth of the 2pM plane shown in left column in the same hybrid 2pM–MesoLF recording as in left column. Right column: Neuronal activity traces corresponding to circles in left and middle column panels, as used for performance quantifications, in experimental functional ground truth (blue traces, corresponding to blue circles in middle column panel), recorded by standard 2pM, analyzed using CaImAn followed by human annotation, and simultaneously acquired LFM recordings, analyzed using MesoLF (red traces, corresponding to red circles in middle column panel), for same two depths as in left column. Solid lines: denoised, shaded lines: raw.

(b) Neuron detection scores precision, sensitivity and F-score achieved by MesoLF on experimental "temporally interleaved" functional verification dataset as a function of depth. Shaded areas: mean ± SD; data from n = 34 recordings, each containing 45 ± 24 (mean ± SD) ground truth active neurons in 280 × 280 µm planar 2pM FOV.

(c) Distributions of lateral neuron localization errors between MesoLF-extracted neuron positions and experimental functional “temporally interleaved” ground truth. White circle: median. Thick grey vertical line: Interquartile range. Thin vertical lines: Upper and lower proximal values. Transparent blue disks: data points. Transparent violin-shaped area: Kernel density estimate of data distribution. n = 1146 neuron pairs.
(d) Distributions of temporal correlations between experimental “temporally interleaved” ground truth activity traces and matched MesoLF traces versus depth. Violin plot elements as in **c**. n = 1146 neuron pairs.
(e) Mean pairwise correlation between all pairs of traces in “temporally interleaved” experimental functional ground truth (blue line) and mean pairwise correlation between corresponding pairs of MesoLF-extracted traces (red line) as a function of lateral distance between the neurons in the pairs. No substantial change in excess correlation, i.e., in the difference between MesoLF-extracted correlation and ground truth correlation, is observable across all pair distances. Shaded areas: Mean ± SD.
(f) Distributions of excess correlation between pairs of neuronal traces in experimental “temporally interleaved” ground truth and corresponding pairs of MesoLF-extracted traces, as a function of depth. White circle: median. Thick grey vertical line: Interquartile range. Thin vertical lines: Upper and lower proximal values. Violin-shaped area: Kernel density estimate of data distribution. n = 50,904 neuron pairs.
(g) Transient extraction scores precision, sensitivity and F-score achieved by MesoLF on experimental “temporally interleaved” functional verification dataset as a function of depth. Transients identified by human annotation of a random subset of n = 136 paired neuron traces (150 s), both in the MesoLF and the 2pM data. Random subset from a total population of 1100 paired neuron traces from 34 recordings across depths 50–400 μm. Individual recordings are 600 seconds long, contain 45 ± 24 (mean ± SD) ground truth active neurons and 291 ± 170 ground truth transients).